

Mitigation of Magnetic Flux Trapping in Superconducting Electronics Using Moats

Rohan T. Kapur,^{*} Sergey K. Tolpygo,[†] Alex Wynn, Pauli Kehayias, Adam A. Libson, Collin N. Muniz, Michael J. Gold, Justin L. Mallek, Danielle A. Braje, and Jennifer M. Schloss
MIT Lincoln Laboratory, Lexington, MA 02421, USA

(Dated: February 23, 2026)

Magnetic flux (vortex) trapping remains a major obstacle to very large scale integration in superconducting electronics. Moats — etched regions in circuit layers placed in ground planes and around critical circuitry — offer a simple passive approach to sequester flux. Here, we systematically examine the effectiveness of moat arrays in superconducting niobium films as a function of geometry (size, shape, and density) and background magnetic field. By measuring the vortex expulsion field, we estimate the flux saturation number and flux trapping temperature for a range of geometries. We find that many moat designs effectively sequester flux in magnetically shielded environments ($< 1 \mu\text{T}$), with high-aspect-ratio rectangular “slit” moats providing the strongest mitigation at minimal area cost. However, our measurements show that moats alone do not eliminate flux trapping in non-ideal films, as vortices can preferentially pin at material defects. These results provide design guidance for flux mitigation in superconducting integrated circuits and highlight the need for combined optimization of circuit geometries and materials.

I. INTRODUCTION

Superconductor classical electronics remain among the most compelling alternatives to traditional complementary metal oxide (CMOS) electronics, offering orders of magnitude improvements in energy efficiency and clock speeds [1–3]. Despite these advantages, the commercial viability of superconductor electronics (SCE) remains limited by scalability challenges, with current integration densities being 3–4 orders of magnitude lower than those achieved in CMOS technologies [4–9]. One significant factor constraining scaling is magnetic flux trapping, a phenomenon that is unique to SCE and distinct from conventional scaling barriers such as heat dissipation and fabrication feature size [10–13].

SCE typically use thin-film Nb, NbN, and NbTiN, all type-II superconductors, for their relatively high superconducting critical temperature, T_c , large critical current densities and high critical magnetic fields, good chemical and mechanical stability, and processing advantages relative to other superconductors [14–19]. When a type-II superconducting film is subjected to a residual magnetic field, B_r , larger than its critical magnetic field, B_{c1} , or is cooled through the superconducting critical temperature in the presence of any residual magnetic field ($B_r \neq 0$), it can trap quantized magnetic flux in the form of vortices, which can interfere with and even completely compromise circuit operation. Various strategies have been proposed and implemented to mitigate flux trapping, including operating in a magnetically shielded environment, applying thermal gradients to drive flux away from critical circuitry [20, 21], defluxing and vortex ratcheting with AC fields [22, 23], and using etched structures in superconducting films to sequester flux away from circuitry. The latter includes slots, slits, and circular or

square holes surrounding or dispersed in the circuitry and ground planes, which are often referred to as moats or antidots [24–29]. However, a comprehensive, universally effective solution for flux trapping in circuits has yet to be found.

Introducing moats into superconducting circuits, if fully effective, would constitute the simplest practical solution to flux trapping, requiring no active circuitry to function. Whereas many prior studies of moat arrays have focused on increasing vortex pinning and high-field behavior [30–36], we evaluate the effectiveness of moat arrays in maintaining a vortex-free (Meissner) state of films cooled in low background magnetic fields ($B_r \leq 10 \mu\text{T}$), typical for superconductor electronics operation. The goal is to engineer moat arrays that achieve strong flux mitigation, while also minimizing the fractional area occupied by moats.

We analyze the effectiveness of moats at mitigating trapped flux by measuring the vortex expulsion field as a function of moat number density and geometry in single-layer Nb films typical of SCE ground planes. Ground planes are generally the dominant flux-trapping regions in SCE circuits due to their large, continuous area [4, 6, 10, 27]. The vortex expulsion field, B_{exp} , is the maximum background magnetic field in which an ideal, defect-free superconducting structure can be cooled through T_c without forming vortices, and thus represents an approximate upper bound on B_r before vortex-induced effects on circuit operation must be considered. Ideally, all circuit elements would be designed with expulsion fields larger than the operating background field, rendering flux trapping irrelevant.

We show that many existing moat designs trap the majority of vortices in $B_r \lesssim 10 \mu\text{T}$ with rectangular “slit” moats (aspect ratio ≥ 30) offering the most effective geometry for strong flux mitigation at a small area footprint. Our results indicate, however, that the effectiveness of moats in non-ideal films is fundamentally constrained by vortex pinning, wherein magnetic flux be-

^{*} rohan.kapur@ll.mit.edu

[†] sergey.tolpygo@ll.mit.edu

comes trapped on microscopic defects within the superconducting film unable to reach moats. This vortex trapping on defects can occur even at very low background fields ($B_r \lesssim 1 \mu\text{T}$), limiting the ability of moats to fully eliminate trapped flux and indicating the need for additional mitigation strategies.

II. RESULTS

A. Square Moat Arrays

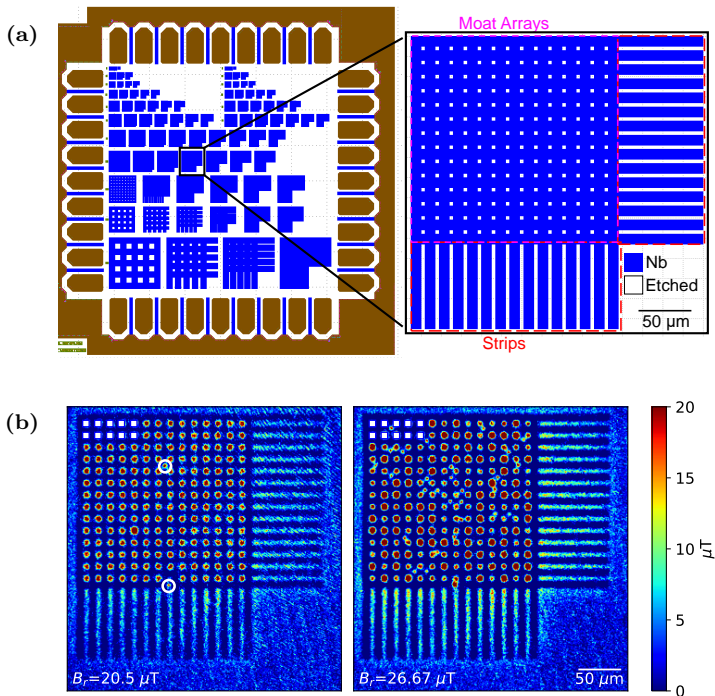


FIG. 1: (a) Layout of test chip used to characterize flux trapping in square moat (antidot) arrays. The spacing between moats varies across rows (0.5–80 μm), while the moat side length varies across columns (1–80 μm). The highlighted region shows the array with moat side length $a = 4 \mu\text{m}$ and spacing $s = 10 \mu\text{m}$. (b) Magnetic images of the $a = 4 \mu\text{m}$, $s = 10 \mu\text{m}$ array at $B_r < B_{\text{exp}}^{\text{meas}}$ (left) and $B_r > B_{\text{exp}}^{\text{meas}}$ (right). Vortices that first appear below $B_{\text{exp}}^{\text{meas}}$ are circled in white (left). Across temperature cycles and background fields, vortices consistently nucleate at these locations.

To systematically characterize moat effectiveness, we measured B_{exp} of Nb square moat arrays — thin-film Nb squares patterned with two-dimensional square lattices of square holes (moats) — as a function of moat side length $a_x = a_y = a$ and spacing $s_x = s_y = s$ (pitch $p_x = a_x + s_x$, $p_y = a_y + s_y$, and $p = a + s$) (see Fig. 1). These arrays are representative of typical ground-plane architectures in superconducting integrated circuits, which are composed of large, periodic moat arrays patterned into the electrically connected circuit ground planes [10].

For this study, we fabricated 5 mm \times 5 mm test chips containing $d = 200 \text{ nm}$ thick Nb films patterned with square arrays of square moats with a ranging from 0.5 to 80 μm and s ranging from 1 to 80 μm , shown in Fig. 1(a). Nb films were deposited on 200-mm Si wafers coated with 100 nm PECVD SiO_2 , using Nb deposition and etching parameters identical to the MIT LL SFQ5ee process [37].

We characterized B_{exp} of moat arrays with a and s ranging from 0.5 to 30 μm and 4 to 40 μm , respectively, and $a \leq s$. The measurements were performed by field cooling the arrays in various B_r and taking magnetic images of the resultant flux distribution. Magnetic images were acquired using a cryogenic widefield nitrogen-vacancy (NV) diamond microscope, which provides quantitative maps of the out-of-plane magnetic field with micron-scale spatial resolution and sensitivity sufficient to resolve individual vortices over millimeter-scale areas from room temperature down to $\sim 5 \text{ K}$ [38]. From the images, the vortex areal density, n_v , was extracted as a function of B_r .

Based on the results, we observed two characteristic fields, B_1 and $B_{\text{exp}}^{\text{meas}}$. The first field, B_1 , is defined as the background field B_r above which vortices first appear in the film outside the moats. Across multiple cooldowns, these first few vortices always appear at the same locations in the film, indicating that they either nucleate or become pinned at these locations. These sites likely correspond to defects in the film acting as strong vortex pinning centers.

We define the measured expulsion field, $B_{\text{exp}}^{\text{meas}}$, of each moat array as the onset of a linear increase in vortex areal density with B_r , where $n_v = m(B_r - B_{\text{exp}}^{\text{meas}})$. We observe the slope m varies slightly between arrays but remains $\sim \Phi_0^{-1}$, where $\Phi_0 = h/2e \approx 2.07 \times 10^{-15} \text{ T} \cdot \text{m}^2$, the magnetic flux quantum. Hereafter, we will analyze $B_{\text{exp}}^{\text{meas}}$ of the measured moat arrays as it likely characterizes the expulsion field of an ideal patterned film, whereas B_1 is more dependent on material quality, film defects, and non-idealities rather than film geometry. Example measurements of the square moat arrays can be found in Fig. 1 and 3(a).

B. Rectangular Moat Arrays

Square moat arrays enable direct comparison of the effects of moat spacing and size on the vortex expulsion field, but they are not necessarily commensurate with circuit design constraints or represent optimal geometries, which may be rectangular ($a_x \neq a_y$) or have anisotropic spacing ($s_x \neq s_y$). For example, SCE devices with rectangular moat arrays in ground planes have demonstrated similarly robust low-field operation while occupying less area [10]. To study rectangular moat arrays, we fabricated a second test chip under the same processing conditions as the square-moat chip, with moat arrays identical to those in the largest operational SCE circuits fabricated in the MIT LL SFQ5ee process [10, 37]. The chip con-

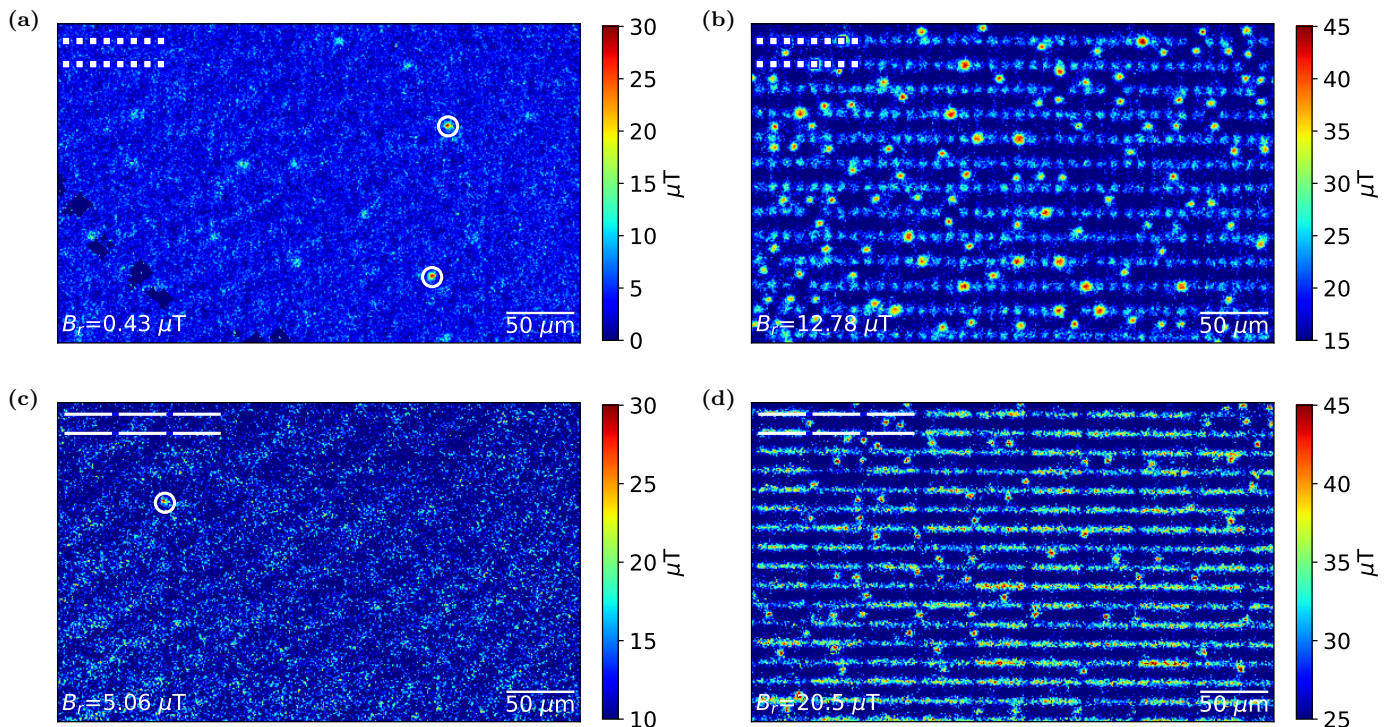


FIG. 2: (a)–(b) Example images of a moat array with $a_x = a_y = 4 \mu\text{m}$, $s_x = 6 \mu\text{m}$, and $s_y = 14 \mu\text{m}$. (c)–(d) Example images of a moat array with $a_x = 36 \mu\text{m}$, $a_y = 1 \mu\text{m}$, $s_x = 4 \mu\text{m}$, and $s_y = 13 \mu\text{m}$. In each image, the first few moats in the upper left are marked (white squares in (a)–(b), white stripes in (c)–(d)), and the first vortices to appear in the film are circled in white. These vortices reproducibly emerge at the same locations across temperature cycles, indicating nucleation and/or pinning at defect sites.

tained 10 distinct rectangular moat arrays which can be classified in two groups: square moats with anisotropic spacing ($a_x = a_y$, $s_x \neq s_y$, see Fig. 2(a)–(b)) and rectangular moats with anisotropic spacing ($a_x \neq a_y$, $s_x \neq s_y$, see Fig. 2(c)–(d)). We measured the $n_v(B_r)$ dependence and vortex expulsion field of each array with the spacing s_x/s_y and moat aspect ratios a_x/a_y ranging from 0.07 to 0.88 and 1 to 65, respectively. As in the square moat arrays, a small number of vortices appear at $B_r < B_{\text{exp}}^{\text{meas}}$ in all measured rectangular arrays, consistently at the same spatial locations and likely due to film non-idealities. Example images of flux distribution in the rectangular moat arrays and expulsion field measurements are in Fig. 2 and 3(b)–(c), while information about each measured rectangular moat array can be found in Table I.

III. DISCUSSION

The simplest model for the vortex expulsion field assumes that all flux threading a unit cell of area $p_x p_y$ in the normal state, $B_r p_x p_y$, is expelled into the single moat it contains upon cooling through T_c , and that each moat can hold at most N_{Φ_0} flux quanta; see Sec. VI A. For an individual moat, N_{Φ_0} is an integer dependent on the moat and array geometry. Under this assumption, vortices appear in the film only if $B_r n_{\text{moat}}/\Phi_0 > N_{\Phi_0}$, which

a_x (μm)	a_y (μm)	s_x (μm)	s_y (μm)	Moat Area	$B_{\text{exp}}^{\text{meas}}$ (μT)
3	3	7	14	5.3%	9.3(6)
3	3	12	14	3.5%	6.4(5)
4	3	14	16	3.5%	4.3(4)
4	4	6	14	8.9%	10.0(11)
4	4	12	14	5.6%	6.5(6)
4	4	14	16	4.4%	4.3(4)
5	5	5	14	13.2%	8.8(5)
9	0.3	1	14	1.8%	13(1)
19.5	0.3	1	14	1.9%	15.9(4)
36	1	4	13	6.4%	16.3(4)

TABLE I: Geometries and measured expulsion fields of all measured rectangular moat arrays. The measured geometries correspond to the moat geometries used in the largest operational SCE circuits fabricated in the MIT LL SFQ5 process [10, 37].

gives the expulsion field of an array as

$$B_{\text{exp}} = \langle N_{\Phi_0} \rangle \Phi_0 n_{\text{moat}}, \quad (1)$$

where $\langle N_{\Phi_0} \rangle$ is the average flux per moat in the array and n_{moat} is the moat areal density.

In the measured films, $n_{\text{moat}} = (p_x p_y)^{-1}$ because $L, W \gg p_x, p_y$, where L and W are the dimensions of the array. The finite film extent and material defects can modify $B_{\text{exp}}^{\text{meas}}$ relative to Eq. 1, as flux may be ex-

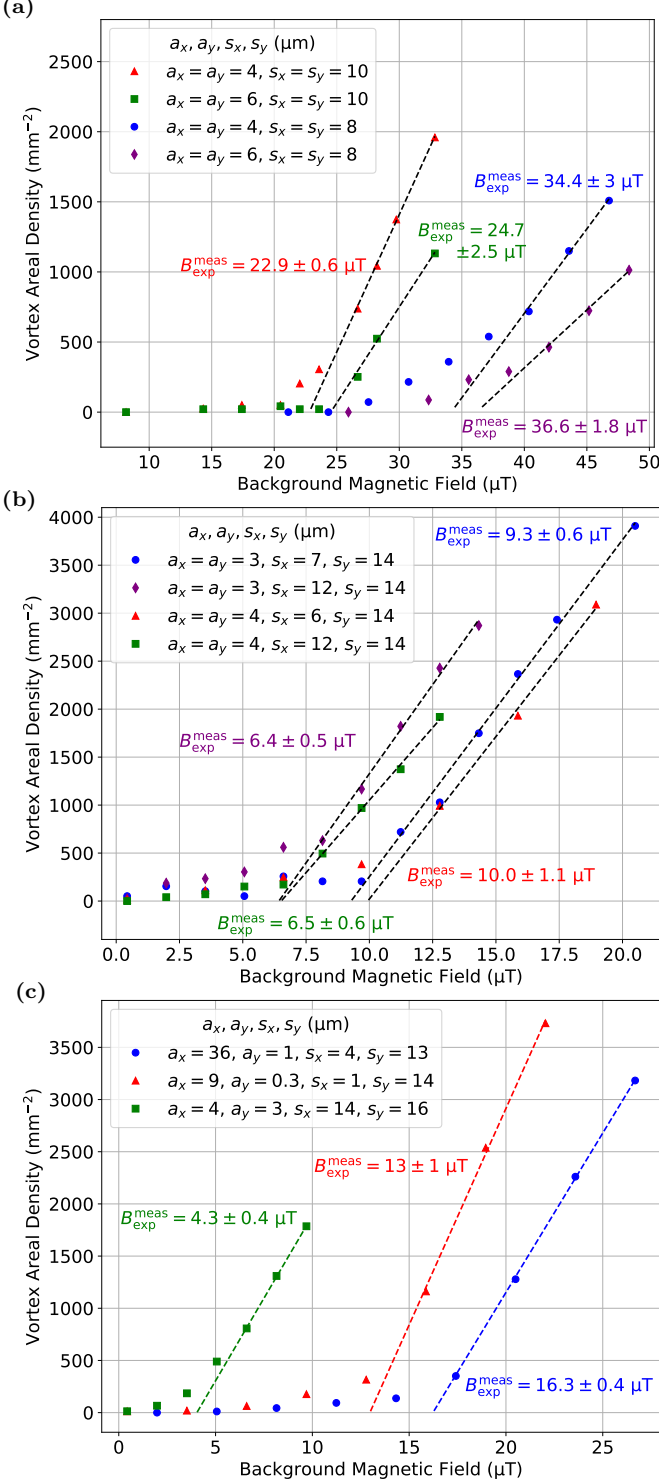


FIG. 3: Example expulsion-field measurements for (a) square moat arrays ($a_x = a_y, s_x = s_y$), (b) square arrays with anisotropic spacing ($a_x = a_y, s_x \neq s_y$), and (c) rectangular arrays with anisotropic spacing ($a_x \neq a_y, s_x \neq s_y$). For each array, the vortex areal density $n_v(B_r)$ is obtained by imaging the vortex distribution at each B_r , and $B_{\text{exp}}^{\text{meas}}$ is extracted from the onset of a linear regime in $n_v(B_r)$ by extrapolating to $n_v = 0$ (with slope m varying slightly between arrays but remaining $\sim \Phi_0^{-1}$). We find $B_{\text{exp}}^{\text{meas}}$ depends most strongly on moat spacing, with a smaller but nontrivial dependence on moat size and shape. In all cases, $n_v \neq 0$ at $B_{\text{exp}}^{\text{meas}}$, as vortices appearing below this field nucleate and/or pin reproducibly at defect sites in the film.

pelled to the film edges or trapped on defects rather than solely accommodated by the moats. Consequently, N_{Φ_0} need not be uniform across unit cells and $\langle N_{\Phi_0} \rangle$ may deviate slightly from an integer. For the measured arrays ($W \times L \geq 100 \times 100 \mu\text{m}^2$), these effects are small compared to the array-induced behavior, consistent with the observed clustering of $\langle N_{\Phi_0} \rangle$ near integer values. The influence of defects is further accounted for by our use of $B_{\text{exp}}^{\text{meas}}$ rather than B_1 (see Sec. II).

In Figure 4, $B_{\text{exp}}^{\text{meas}}$ is plotted vs $\langle N_{\Phi_0} \rangle \Phi_0 n_{\text{moat}}$ at $\langle N_{\Phi_0} \rangle = 1$. Fig. 4 shows that, at fixed moat density, the amount of flux per moat at the expulsion field depends strongly on moat shape and size. For example, at comparable moat densities, $a_x = 36 \mu\text{m}, a_y = 1 \mu\text{m}$ slits trap $\sim 5 \times$ more flux than $a = 4 \mu\text{m}$ squares. The data also indicate that $\langle N_{\Phi_0} \rangle$ depends strongly on moat spacing (pitch), with dense arrays of moats trapping significantly more flux than sparse arrays. Among the measured moat arrays, slit moats appear to be the most attractive for SCE applications due to their small area footprint and ability to trap multiple flux quanta.

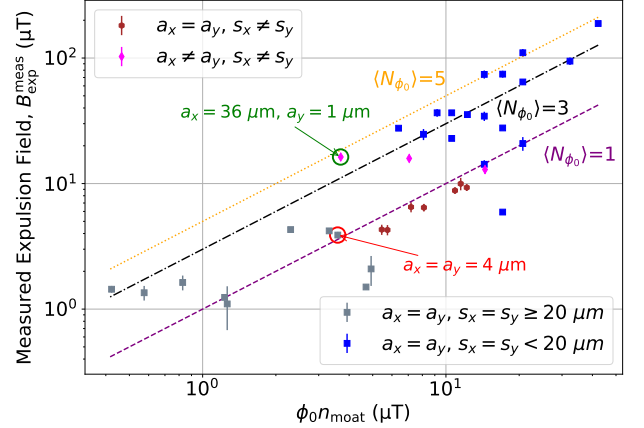


FIG. 4: Measured expulsion field vs. $\langle N_{\Phi_0} \rangle \Phi_0 n_{\text{moat}}$, assuming $\langle N_{\Phi_0} \rangle = 1$ (Eq. 1). The purple, black, and orange lines indicate the expected behavior for $\langle N_{\Phi_0} \rangle = 1, 3, \text{ and } 5$, respectively. Square arrays with $s \geq 20 \mu\text{m}$ and arrays with anisotropic spacing agree well with $\langle N_{\Phi_0} \rangle = 1$. For $s < 20 \mu\text{m}$ and highly asymmetric moats ($a_x/a_y \geq 30$), the data instead fall within $1 \leq \langle N_{\Phi_0} \rangle \leq 5$, indicating multiple flux quanta per moat before vortices enter the film. For example, at comparable moat densities, $a_x = 36 \mu\text{m}, a_y = 1 \mu\text{m}$ slits trap $\sim 5 \times$ more flux than $a = 4 \mu\text{m}$ squares.

To better understand the expulsion field of films with periodic arrays of narrow slits, we consider the slits in the idealized limiting case $a_x \rightarrow p_x$. In this limit, the spacing between the moats along one dimension approaches zero and the initial superconducting film breaks into a set of parallel horizontal strips with width s_y and spacing a_y . B_{exp} for a single long strip with width w has been extensively studied both theoretically and experimentally

and is given by

$$B_{\text{exp}} = \beta \Phi_0 / w^2, \quad (2)$$

where β is a parameter that assumes different values in different theoretical models and experimentally was found to weakly depend on the superconducting film parameters [12, 38–43]. Assuming the presence of adjacent strips does not significantly affect B_{exp} , B_{exp} for films with narrow slits with $a_x \rightarrow p_x$ would scale as

$$B_{\text{exp}} = \beta \Phi_0 / s_y^2, \quad (3)$$

since s_y is the effective strip width for the array of narrow slits with $p_x - a_x \ll a_x$ along the x-direction.

A two-dimensional array of moats can be approximated by either horizontal strips with width s_y in the limit $a_x/p_x \rightarrow 1$, or vertical strips with width s_x in the limit $a_y/p_y \rightarrow 1$. In the latter case, s_x would replace s_y in Eq. 3. The simplest interpolation between these two dependencies is

$$B_{\text{exp}} = \frac{\beta \Phi_0}{s_x^2 + s_y^2}, \quad (4)$$

where $s_x^2 + s_y^2$ represents the square of the widest part of the film between moats.

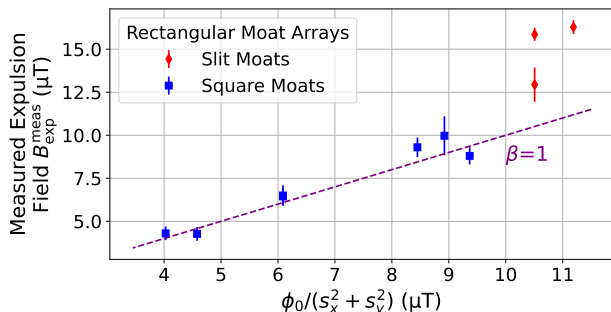


FIG. 5: Measured expulsion field of the rectangular moat arrays vs. the expected expulsion field assuming the scaling laws described in Eq. 4 and $\beta = 1$, which approximate the expulsion field based on the moat spacing. For reference, the purple line illustrates the expected behavior for $\beta = 1$. The data shows good agreement for $\beta \approx 1$ for the square moats with anisotropic spacing, but deviates from this scaling for the slit moats, indicating a non-trivial dependence on moat size and aspect ratio. For simplicity, we have included the measured $a_x = 4 \mu\text{m}$, $a_y = 3 \mu\text{m}$, $s_x = 14 \mu\text{m}$, and $s_y = 16 \mu\text{m}$ moats in the square rather than slit dataset, as its aspect ratio is much closer to that of squares ($a_x/a_y = 1$) than slits ($a_x/a_y \geq 30$).

In Fig. 5, $B_{\text{exp}}^{\text{meas}}$ of the rectangular moat arrays is plotted vs. the scaling field $\Phi_0/(s_x^2 + s_y^2)$ in Eq. 4 at $\beta = 1$. As seen in Fig. 5, describing the data by Eq. 4 requires different values of β for different types of moats, showing

good agreement with $\beta \approx 1$ for the square moat arrays with anisotropic spacing, but deviating from this scaling for the slit geometries with $s_x \ll s_y$.

From the already presented data, it is unclear which of the scaling functions, Eq. 1 or Eq. 4, better describes the data overall. Neither function captures the dependence of the expulsion field on moat size; each accounts for only moat density or spacing, and neither shows consistent agreement with all the data. To gain some insight on these issues, we focused specifically on the expulsion field in the square moat arrays, where $s_x = s_y = s$ and $a_x = a_y = a$, which offer a simpler case to analyze.

The average number of flux quanta per moat, defined in Eq. 1, is

$$\langle N_{\Phi_0} \rangle = \frac{B_{\text{exp}}^{\text{meas}}}{n_{\text{moat}} \Phi_0}, \quad (5)$$

and is plotted in Fig. 6 versus a/p and a/s for all measured square arrays. Although individual moats must contain integer number of flux quanta, the array-averaged value $\langle N_{\Phi_0} \rangle$ can deviate slightly due to edge effects and pinning/nucleating on film defects (see Eq. 1). Nevertheless, the data cluster near integer values of $\langle N_{\Phi_0} \rangle$, indicating that these deviations are small.

Figure 6 shows that arrays with large a/s (or a/p) trap multiple flux quanta per moat, whereas small a/s (or a/p) arrays are only singly or partially occupied before vortices enter the film. Accordingly, $\langle N_{\Phi_0} \rangle$ increases approximately linearly with a/s , favoring closely spaced, large moats for flux sequestration, albeit at the cost of reduced useful circuit area and increased moat–circuit coupling (see Sec. VI A). A linear fit of the data in Fig. 6 gives $\langle N_{\Phi_0} \rangle = 4.7(a/s) + 0.2$. Neglecting the small offset yields the approximate scaling

$$B_{\text{exp}}^{\text{meas}} \approx 4.7 \left(\frac{a}{s} \right) n_{\text{moat}} \Phi_0, \quad (6)$$

indicating that the expulsion field depends on both moat size (a/s) and spacing/density $[(s_x^2 + s_y^2)^{-1}]$.

Figure 7 examines the moat size and spacing dependencies by plotting $B_{\text{exp}}^{\text{meas}}$ versus spacing for all square moat arrays using the data binned by a/s . While the full dataset does not agree with Eq. 4, the binned data show excellent agreement, further indicating that the expulsion field depends on *both* moat size and spacing.

Based on the above discussion and measured dependencies described by Eq. 4 and Eq. 6, and further verified in Fig. 7, we propose an empirical model to describe the expulsion field behavior of moats across all measured geometries characterized by

$$B_{\text{exp}} = \frac{\gamma \Phi_0 f(a_x, a_y, s_x, s_y)}{s_x^2 + s_y^2}, \quad (7)$$

where γ is a dimensionless constant and $f(a_x, a_y, s_x, s_y)$ is a function describing the expulsion field moat size dependence. At present, it is unclear to us what the exact function or appropriate scaling form of $f(a_x, a_y, s_x, s_y)$

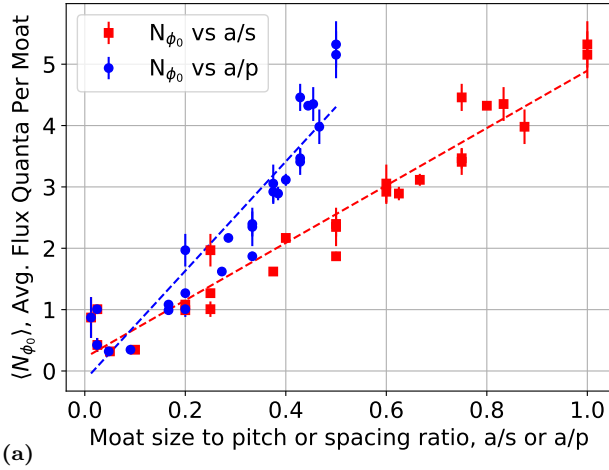


FIG. 6: $\langle N_{\Phi_0} \rangle$, the average amount of flux per moat, vs. the moat size to pitch and moat size to spacing ratios for the measured square moat arrays. The data show good agreement with a linear dependence of $\langle N_{\Phi_0} \rangle$ on the moat size to spacing ratio, while the exact scaling behavior of $\langle N_{\Phi_0} \rangle$ vs. a/p is unclear. The best linear fit for $\langle N_{\Phi_0} \rangle$ vs. a/s gives $\langle N_{\Phi_0} \rangle = 4.7(\frac{a}{s}) + 0.2$.

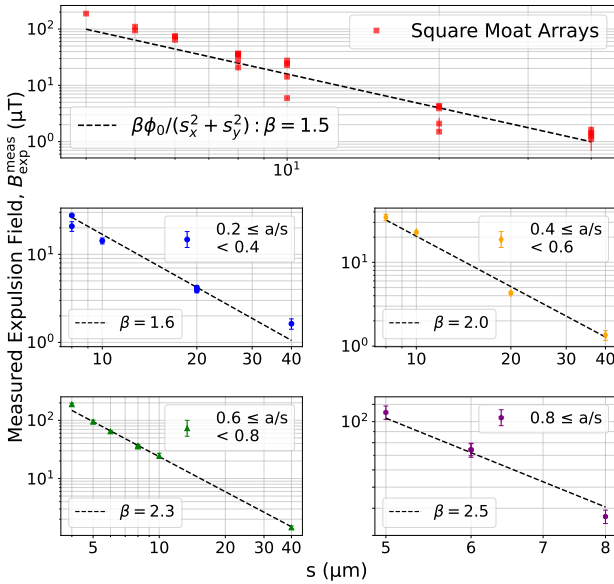


FIG. 7: Expulsion field $B_{\text{exp}}^{\text{meas}}$ vs. moat spacing for square moat arrays in Nb films. Dash lines are fits to Eq. 4, with β as a fit parameter. The top plot (a) shows all the data, which overall do not agree with Eq. 4, while data binned in a/s values show good agreement with Eq. 4 for each bin, indicating the $B_{\text{exp}}^{\text{meas}}$ dependence on both the moat spacing and moat size to spacing ratio. The fitted β values for the binned datasets are all order unity, ranging from 1.6 to 2.5.

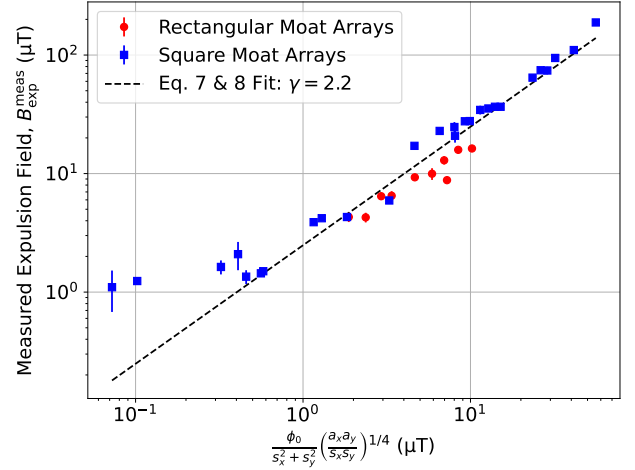


FIG. 8: Expulsion field $B_{\text{exp}}^{\text{meas}}$ vs. proposed scaling relationship described in Eq. 7 and Eq. 8. The data was fit to Eq. 7 and Eq. 8 with γ as a fitted parameter with the best fit producing $\gamma = 2.2$. The empirical model shows reasonable agreement with all measured data, except at very large spacings between moats, $s_x, s_y \gtrsim 40 \mu\text{m}$, but does not necessarily represent an exact model.

is. We find that Eq. 7 provides a reasonable description of the entire set of the obtained data, using an empirical function

$$f(a_x, a_y, s_x, s_y) = \left(\frac{a_x a_y}{s_x s_y} \right)^{1/4}, \quad (8)$$

as shown in Fig. 8.

Figure 8 shows good agreement of the proposed scaling form with the data covering more than two orders of magnitude in the expulsion field, and gives $\gamma = 2.2$. The model breaks down for the largest moat spacing, $s = 40 \mu\text{m}$, where all arrays have $B_{\text{exp}}^{\text{meas}} \lesssim 2 \mu\text{T}$, comparable to the $s = 20 \mu\text{m}$ arrays with $a \leq 1 \mu\text{m}$. At $s = 40 \mu\text{m}$, $B_{\text{exp}}^{\text{meas}}$ also shows little dependence on moat size (1.44 ± 0.09 and $1.24 \pm 0.07 \mu\text{T}$ for $a = 30$ and $1 \mu\text{m}$, respectively). This is unexpected, since capturing vortices between widely spaced small moats should become progressively more difficult as the vortex–moat interaction diminishes with distance and decreasing moat size. Instead, we observe a plateau in $B_{\text{exp}}^{\text{meas}}$ versus moat spacing and size at $s = 40 \mu\text{m}$, also visible in Fig. 6 at very small a/s .

Apart from the $s = 40 \mu\text{m}$ moats, both the measured square and rectangular moat arrays show very similar scaling behavior in agreement with our proposed empirical model with only a slight difference in the global offset, likely due to a larger overall size of the rectangular moat arrays. Overall, the data and model indicate that closely spaced moats with large perimeters and aspect ratios provide the highest expulsion field values.

IV. CONCLUSION

Magnetic flux trapping remains a critical hurdle in preventing superconducting electronics from reaching very large scale integration. Moats represent one of the simplest practical flux mitigation strategies, requiring only etched holes in the superconducting films and no active circuitry. We have evaluated the effectiveness of various moat geometries in removing magnetic flux by measuring the vortex expulsion field of Nb films with patterned arrays of moats in a wide range of moat sizes, spacings, and aspect ratios. We have found that arrays of closely-spaced, large-perimeter moats, such as long slits or large squares, provide the highest expulsion field values, consistent with the empirical scaling described by Eqs. 7 and 8. These geometries can trap multiple flux quanta per moat before vortices enter the film and can attract vortices over distances comparable to the moat dimensions. In contrast, sparse arrays of small square (or rectangular) moats ($a_x, a_y \lesssim 5 \mu\text{m}$ with spacings $s \geq 2a$) typically trap only a single flux quantum per moat before vortices appear in the film, resulting in substantially lower expulsion fields.

For superconducting integrated circuits, the data suggest the use of narrow slit-type moats with densities commensurate with the expected background field and circuit layout constraints. For a given moat density, slit-type moats can trap more flux quanta than square moats, while also occupying less circuit area, enabling high expulsion fields without excessive loss of usable circuit area. For circuit designs in the SFQ5ee process using 200-nm-thick Nb films, we recommend a moat density of $n_{\text{moat}} \geq B_r/\Phi_0$, and the maximum moat spacing of approximately $14 \mu\text{m}$; see Sec. VIB for details. For any designed array and moat geometry, the vortex expulsion field can be estimated using Eqs. 7 and 8 with $\gamma \approx 2$. Among the measured geometries, the $a_x = 9 \mu\text{m}, a_y = 0.3 \mu\text{m}, s_x = 1 \mu\text{m}, s_y = 14 \mu\text{m}$ array (see Fig. 3(c)) provides an attractive balance between expulsion field ($> 10 \mu\text{T}$) and footprint (1.8% of a unit cell). The $a_x = 36 \mu\text{m}, a_y = 1 \mu\text{m}, s_x = 4 \mu\text{m}, s_y = 13 \mu\text{m}$ geometry (also used in [4, 6, 10]) offers even higher expulsion field ($16.3 \mu\text{T}$ vs. $13 \mu\text{T}$) at the cost of increased area (6.4% of a unit cell). Further exploration of high-aspect-ratio slit geometries is therefore well motivated, particularly in regimes approaching their practical limits, while remaining commensurate with circuit design constraints.

For circuits operating in magnetically shielded environments ($B_r \lesssim 1 \mu\text{T}$), most moat geometries are capable of sequestering the majority of flux expelled during cooldown. However, the data show that *moats alone are insufficient in eliminating all trapped flux in non-ideal films*. Whereas the measured expulsion field $B_{\text{exp}}^{\text{meas}}$ characterizes the geometry-dependent threshold at which vortex density $n_v(B_r)$ begins to grow proportionally to B_r/Φ_0 , across all geometries we have observed a few isolated vortices appearing at lower fields, always at repro-

ducible locations across multiple cooldowns, consistent with nucleation and/or pinning at film defects. An example of this can be seen in Fig. 3(c) for the array with $a_x = 9 \mu\text{m}, a_y = 0.3 \mu\text{m}, s_x = 1 \mu\text{m}, s_y = 14 \mu\text{m}$, which exhibits $B_{\text{exp}}^{\text{meas}} > 10 \mu\text{T}$, but a few vortices observed in the film at $B_r < 1 \mu\text{T}$. Thus, while moats are essential in helping circuits to expel most of the initially threading flux, material defects in non-ideal films may often prevent the complete flux elimination in moat-guarded circuits.

Therefore, mitigating parasitic flux trapping requires optimization of both the moat design and materials used in superconducting electronics, especially in wide ground planes. The emphasis should be on increasing the field at which vortices become trapped on pinning sites and can no longer be sequestered into the moats (field B_1 in this work), i.e., on reducing strong vortex pinning but without compromising the critical currents required for circuit operation. Future work will investigate the material dependence of $B_{\text{exp}}^{\text{meas}}$ and B_1 , the role of film defects and other sources of flux trapping, and additional flux mitigation strategies. A comprehensive solution will likely require the combined optimization of magnetic shielding, moat geometry, superconducting film materials and fabrication, and potentially active circuitry to remove trapped flux.

V. ACKNOWLEDGEMENTS

We thank Tom Osadchy for assistance with diamond growth; Peter O'Brien, Jon Wilson, and Matthew Ricci for help with diamond coating; and Anil Mankame, Tom Grasso, George Haldeman, Nate O'Connor, John Cummings, Neel Parmar, Ryan Johnson, and Andrew Maccabe for assistance with instrument design, assembly, and testing. We are grateful to Ravi Rastogi and David Kim for overseeing fabrication of the Nb films and test structures used in this work, and to Rabindra Das for help with packaging. We thank Andrew Wagner, Neel Parmar, Michele Kelley, and Logan Bishop-Van Horn for helpful discussions. Rohan Kapur thanks John Kim for continued assistance.

This material is based upon work supported under Air Force Contract No. FA8702-15-D-0001 or FA8702-25-D-B002. Any opinions, findings, conclusions or recommendations expressed in this material are those of the authors and do not necessarily reflect the views of the U.S. Air Force. Notwithstanding any copyright notice, U.S. Government rights in this article are defined by DFARS 252.227-7013 or DFARS 252.227-7014 as detailed above. Use of this article other than as specifically authorized by the U.S. Government may violate any copyrights that exist in this article. The U.S. Government is authorized to reproduce and distribute reprints for Governmental purposes notwithstanding any copyright annotation thereon.

VI. APPENDIX

A. Trapped Flux in an Isolated Moat

The problem of trapping flux quanta in openings (cylindrical pores, columnar defects, antidots) in superconductors has been studied theoretically and experimentally since the pioneering work by Mkrtychyan and Schmidt [44, 45], who showed that an opening in a superconductor always has an attractive potential for vortices, similar to the interaction with an image antivortex, while the potential of the opening filled with one flux quanta is attractive at small distances and repulsive at large distances from the opening. They showed that the number of flux quanta at which the potential becomes repulsive at all distances, i.e., the maximum number of flux quanta that can be attracted and trapped into a cylindrical opening with radius $R \ll \lambda(T)$, called the saturation number N_s , is given by

$$N_s(T) = \frac{R^2}{\xi(T)^2 + 2\xi(T)R}, \quad (9)$$

which is approximated by $R/2\xi(T)$ for $R \gg \xi(T)$, where $\lambda(T)$ and $\xi(T)$ are the temperature-dependent magnetic field penetration depth and coherence length, respectively; see also [46–49] and references therein. According to Buzdin [46], the $N_s = 2$ flux state of a circular hole in the film is energetically stable if $R^3 > \xi(T)\lambda(T)^2$. In large magnetic fields, the saturation number changes to approximately $R^2/\xi(T)^2$ due to interaction with (pressure created by) adjacent vortices [50]. Trapping of multiple vortices in dense arrays of circular holes, following roughly the latter dependence, was observed, e.g., in [51]. Calculations in [46–50], assume that the hole filling by flux quanta occurs sequentially, one by one, and use London or Ginzburg-Landau [52] free energy to find the N_s value at which the hole potential changes from attractive to repulsive for the next, N_{s+1} , vortex at any vortex-hole separation. This scenario, however, is unlikely to take place during the superconducting transition of a thin film in a weak perpendicular magnetic field because it implies that the Meissner state of the entire film and vortices with currents circulating on a large $\lambda(T)^2/d$ scale comparable to the spacing between moats and the film width are fully formed at any temperature arbitrarily close to T_c . Instead, magnetic flux is probably pushed gradually out from the film simultaneously with the formation of the macroscopic coherent state and circulating currents.

Regardless of the exact trapping dynamics, the flux saturation number, i.e., the maximum number of flux quanta which can be held in a moat, can be estimated from the fluxoid quantization in superconductors

$$\mu_0\lambda(T)^2 \oint \vec{j}_s \cdot d\vec{l} = N_s \Phi_0 - \oint \vec{A} \cdot d\vec{l}, \quad (10)$$

where \vec{A} is the vector potential of the applied field, \vec{j}_s is the superconducting current density, and contour can

be any closed path in the superconductor. Flux accumulation in the hole (moat) increases the screening current circulating the moat and can proceed until the current density near the moat rim reaches the depairing current density which near the critical temperature is given by the Ginzburg-Landau expression [52–55].

$$j_c^{\text{GL}} = \frac{\Phi_0}{3\sqrt{3}\mu_0\xi(T)\lambda(T)^2}. \quad (11)$$

Very close to T_c , where the penetration depth is very large, $\lambda(T) \gg d$ and $\lambda(T)^2/d \gg R, a, s$, and in very small magnetic fields we can neglect the last term $\oint \vec{A} \cdot d\vec{l}$ in Eq. 10 in comparison to the first term, i.e., we can neglect magnetic field energy in the moat in comparison to kinetic energy of the supercurrent circulating the moat. Then, for a path around the circular hole rim, the current density j_s is constant and, in this simplified model, $N_s = 2\pi R / (3\sqrt{3}\xi(T)) = 1.2R/\xi(T)$, which is just a factor of two larger than the more accurate result of [44] at $R \gg \xi(T)$.

For other moat geometries (squares and slits), j_s is not strictly constant around the moat perimeter and can be found by solving London equations in the Meissner state; see [56, 57]. To get an estimate, we neglect corner effects and assume a constant current density around the perimeter of the square moats and long slits. Then, from Eq. 10 and Eq. 11, the maximum number of flux quanta that can be held in a moat very close to T_c , $N_s \propto P/\xi(T)$ where P is the moat perimeter, with a proportionality coefficient of $1/3\sqrt{3} = 0.19$.

Qualitatively the same result follows from a simple electrical engineering formula $\Phi = LI_{\text{cir}}$ where Φ is the total flux in the moat, L is the moat inductance, and I_{cir} is the total current circulating the moat. Very near T_c , kinetic inductance of the film surrounding the moat $L_k = \mu_0\lambda(T)^2/d$ (per square) is much larger than the moat geometrical inductance, $\simeq \mu_0 a$. Then, the total inductance can be estimated as $L = \mu_0(P/w)\lambda(T)^2/d$ where P/w is the number of squares in the film and w is the typical width of the area in which currents are flowing around the moat; $w \sim s/2$ in arrays. The maximum flux the moat can hold, Φ_{max} , corresponds to the circulating current reaching the critical value $j_c dw$. Using Eq. 11 for j_c , we get the same expression $N_s = \Phi_{\text{max}}/\Phi_0 = kP/\xi(T)$, where k is a numerical coefficient depending on the moat shape. For a square hole with size a , $N_s \sim \frac{0.8a}{\xi(T)}$, and for a long slit with length l , $N_s \sim \frac{0.4l}{\xi(T)}$.

Unfortunately, we do not know at what temperature flux expulsion into the moat occurs and, hence, the value of $\xi(T)$. Nevertheless, we can assume that flux expulsion into the moats occurs at the same temperature regardless of the shape and density of moats. We also assume that the realized N_{Φ_0} value does not change as the film temperature is lowered to the base temperature of the measurements, about 5 K, despite the decrease of $\xi(T)$, because the remaining, not trapped close to T_c , flux becomes immobile as frozen vortices and because the moat

potential becomes repulsive at large distances from the moat. That is, we assume that the flux distribution imaged in the measurements is the frozen snapshot of the process that happened very close to T_c . Then, for sparse arrays, the ratio of N_{Φ_0} for different moat shapes should be equal to the ratio of their perimeters, which can be easily verified experimentally, e.g., using the data in Fig. 3. For instance, for the measured arrays of slits with $a_x = 36, 19.5, 9 \mu\text{m}$, $s_x = 4 \mu\text{m}$ and $s_y = 14 \mu\text{m}$, the average $\langle N_{\Phi_0} \rangle = 5, 2.9$ and 1.15 , respectively, having the ratios $4.3 : 2.5 : 1$ which are very close to the ratios of their perimeters $4 : 2.2 : 1$.

However, for all square moat arrays with $a = 1, 2, 3, 4, 5 \mu\text{m}$ and $p_x \geq 20$ or $p_y \geq 20 \mu\text{m}$, $N_{\Phi_0} = 1$ was found, despite large differences in the moat perimeters; see Fig. 3. That is the measured, actually realized upon field cooling, N_{Φ_0} value is much smaller than the flux saturation value N_s characterizing the moat potential capacity. This indicates that square and small-aspect-ratio rectangular moats filled with just one flux quantum become repulsive and *cannot attract* vortices located at distances comparable to or larger than the moat size a , although they potentially could hold more than one flux quantum. However, closely spaced square moats with spacings $s \leq a$ can attract and hold up to $5\Phi_0$; see Fig. 4 and Fig. 6. This indicates once again the importance of electromagnetic interactions between vortices and moats, and between the adjacent moats, and confirms their short range nature [47], as well as importance of dynamic effects in expelling flux into the moats. For instance, vortices can hardly be attracted from symmetrical positions in the middle between two or four moats, i.e., at distance $a/2$ from the moat side, where the attraction/repulsion forces are balanced.

B. Estimate of Flux Trapping Temperature and Circuit Geometry Recommendations

Linear scaling of N_{Φ_0} with a/s in Fig. 6 indicates that the moat potential, which at small distances decays approximately as $1/r$ for a single circular or square moat (where r is the distance from the moat center) is significantly modified by the presence of adjacent moats, allowing moats in dense arrays to trap more flux quanta per moat than an isolated moat. Empirically, the effective area from which magnetic flux can be swept into the moats of given sizes a_x, a_y and spacings s_x, s_y is given by the scaling functions in Eq. 7 and Eq. 8.

Using the data in Fig. 6, we can estimate the value of $\xi(T)$ at a temperature when flux expulsion from the film and trapping into the moats occurs, T_{exp} . Indeed, sparse ($s \gg a$) arrays trap $N_{\Phi_0} = 1$ down to sizes a_{min} of about

$1 \mu\text{m}$. Then, from Eq. 9, $\xi(T_{\text{exp}}) \approx a_{\text{min}}/4 \approx 0.25 \mu\text{m}$. For our Nb films at 4.2 K, $\xi(4.2\text{K}) = 18 \text{ nm}$ and $T_c = 9.2 \text{ K}$ [38], giving $T_{\text{exp}}/T_c \approx 0.9948$, i.e., flux expulsion and trapping in the moats occurs $\approx 48 \text{ mK}$ below T_c . At this temperature, the Pearl screening length $\Lambda(T) = 2\lambda(T)^2/d$ [58] that sets the range of vortex interactions in thin films is $\Lambda(T_{\text{exp}}) = 3.5 \mu\text{m}$ in 200-nm thick Nb films with $\lambda(0) = 82 \text{ nm}$ [59]. At distances larger than $\Lambda(T)$ currents circulating the vortex decay as r^{-2} [58]. Therefore, moats spaced at $s \gg \Lambda(T_{\text{exp}})$ become ineffective in trapping vortices located between them because similarly quickly decaying with distance attraction force to the moats becomes insufficient to overcome even weak pinning forces created by defects in the film. In practice, the recommended spacing between the moats should be $s \lesssim 4\Lambda(T_{\text{exp}}) \approx 14 \mu\text{m}$ in 200-nm-thick Nb films. It should be scaled proportionally to d^{-1} for thicker or thinner films.

C. Square Moat Array Measurement Data

a (μm)	s (μm)	Moat Area	$B_{\text{exp}}^{\text{meas}}$ (μT)
3	4	18.4%	188(9)
3	5	14.1%	94(6)
5	5	25.0%	110(8)
4	6	16.0%	64.5(20)
5	6	20.7%	74(5)
6	6	25.0%	74(6)
2	8	4.0%	21(3)
3	8	7.4%	27.7(7)
4	8	11.1%	34.4(3)
5	8	14.8%	35.4(13)
6	8	18.4%	36.6(18)
7	8	21.7%	37(3)
1	10	0.8%	5.93(22)
2	10	2.8%	17.1(4)
4	10	8.2%	22.9(6)
6	10	14.1%	24.7(25)
8	10	19.8%	27.62(22)
0.5	20	0.06%	2.1(6)
1	20	0.23%	1.50(7)
4	20	2.8%	3.89(23)
5	20	4.0%	4.20(19)
10	20	11.1%	4.30(17)
0.5	40	0.015%	1.1(4)
1	40	0.06%	1.24(7)
10	40	4.0%	1.63(22)
20	40	11.1%	1.35(18)
30	40	18.4%	1.44(9)

TABLE II: Geometries and measured expulsion fields of all measured square moat arrays.

-
- [1] T. Van Duzer, *Cryogenics* **30**, 980 (1990).
- [2] A. I. Braginski, *Journal of Superconductivity and Novel Magnetism* **32**, 23 (2019).
- [3] R. Bairamkulov and G. De Micheli, *IEEE Circuits and Systems Magazine* **24**, 16 (2024).
- [4] V. K. Semenov, Y. A. Polyakov, and S. K. Tolpygo, *IEEE Transactions on Applied Superconductivity* **27**, 1 (2017).
- [5] S. Nagasawa, T. Satoh, K. Hinode, Y. Kitagawa, and M. Hidaka, *IEEE Transactions on Applied Superconductivity* **17**, 177 (2007).
- [6] V. K. Semenov, Y. A. Polyakov, and S. K. Tolpygo, *IEEE Transactions on Applied Superconductivity* **25**, 1 (2015).
- [7] Q. P. Herr, J. Osborne, M. J. A. Stoutimore, H. Hearne, R. Selig, J. Vogel, E. Min, V. V. Talanov, and A. Y. Herr, *Superconductor Science and Technology* **28**, 124003 (2015).
- [8] M. Hidaka and S. Nagasawa, *IEICE Transactions on Electronics* **E104.C**, 405 (2021).
- [9] C. L. Ayala, T. Tanaka, R. Saito, M. Nozoe, N. Takeuchi, and N. Yoshikawa, *IEEE Journal of Solid-State Circuits* **56**, 1152 (2021).
- [10] E. B. Golden, N. A. Parmar, V. K. Semenov, and S. K. Tolpygo, *IEEE Transactions on Applied Superconductivity* **35**, 1 (2025).
- [11] S. Narayana, Y. A. Polyakov, and V. K. Semenov, *IEEE Transactions on Applied Superconductivity* **19**, 640 (2009).
- [12] M. Washington and T. Fulton, *Applied Physics Letters* **40**, 848 (1982).
- [13] S. Narayana, Y. Polyakov, and V. Semenov, *IEEE Transactions on Applied Superconductivity* **19**, 640 (2009).
- [14] K. K. Likharev, *Physica C: Superconductivity and its applications* **482**, 6 (2012).
- [15] S. K. Tolpygo, *Low Temperature Physics* **42**, 361 (2016).
- [16] S. Tahara, S. Yorozu, Y. Kameda, Y. Hashimoto, H. Numata, T. Satoh, W. Hattori, and M. Hidaka, *IEEE transactions on applied superconductivity* **11**, 463 (2002).
- [17] S. K. Tolpygo, J. L. Mallek, V. Bolkhovskiy, R. Rastogi, E. B. Golden, T. J. Weir, L. M. Johnson, and M. A. Gouker, *IEEE Transactions on Applied Superconductivity* **33**, 1 (2023).
- [18] S. R. Nieto, J. A. Hofer, M. Sirena, and N. Haberkorn, *Physica C: Superconductivity and its Applications* **607**, 1354241 (2023).
- [19] A. Pokhrel, D. P. Lozano, J.-P. Soulié, D. Vangoidsenhoven, S. K. Sarkar, R. K. Saroj, Y. Canvel, V. Renaud, B. Kenens, A. M. Walke, *et al.*, in *2024 IEEE International Electron Devices Meeting (IEDM)* (IEEE, 2024) pp. 1–4.
- [20] I. S. Veshchunov, W. Magrini, S. Mironov, A. Godin, J.-B. Trebbia, A. I. Buzdin, P. Tamarat, and B. Lounis, *Nature communications* **7**, 12801 (2016).
- [21] Q. Geng, H. Minami, K. Chihara, J. Yuyama, and E. Goto, *Journal of applied physics* **72**, 2411 (1992).
- [22] C.-S. Lee, B. Janko, I. Derenyi, and A.-L. Barabási, *Nature* **400**, 337 (1999).
- [23] A. N. Matlashov, V. K. Semenov, and W. H. Anderson, *IEEE Transactions on Applied Superconductivity* **27**, 1 (2017).
- [24] V. K. Semenov and M. M. Khapaev, *IEEE Transactions on Applied Superconductivity* **26**, 1 (2016).
- [25] V. K. Semenov and M. M. Khapaev, *IEEE Transactions on Applied Superconductivity* **26**, 1 (2016).
- [26] S. Bermon and T. Gheewala, *IEEE Transactions on Magnetics* **19**, 1160 (1983).
- [27] M. Jeffery, T. Van Duzer, J. R. Kirtley, and M. B. Ketchen, *Applied Physics Letters* **67**, 1769 (1995).
- [28] C. J. Fourie and K. Jackman, *IEEE Transactions on Applied Superconductivity* **31**, 1 (2021).
- [29] F. Colauto, M. Motta, and W. Ortiz, *Superconductor Science and Technology* **34**, 013002 (2020).
- [30] G. Berdiyrov, M. Milošević, and F. Peeters, *Physical review letters* **96**, 207001 (2006).
- [31] J. Vestgård, V. Yurchenko, R. Wördenweber, and T. Johansen, *Physical Review B—Condensed Matter and Materials Physics* **85**, 014516 (2012).
- [32] D. Priour Jr and H. Fertig, *Physical review letters* **93**, 057003 (2004).
- [33] S. Raedts, A. Silhanek, M. Van Bael, and V. Moshchalkov, *Physical Review B* **70**, 024509 (2004).
- [34] G. Berdiyrov, M. Milošević, and F. Peeters, *Europhysics Letters* **74**, 493 (2006).
- [35] G. R. Berdiyrov, M. V. Milošević, and F. M. Peeters, *Phys. Rev. B* **74**, 174512 (2006).
- [36] A. Silhanek, L. Van Look, R. Jonckheere, B. Zhu, S. Raedts, and V. Moshchalkov, *Physical Review B—Condensed Matter and Materials Physics* **72**, 014507 (2005).
- [37] S. K. Tolpygo, V. Bolkhovskiy, T. J. Weir, A. Wynn, D. E. Oates, L. M. Johnson, and M. A. Gouker, *IEEE Transactions on Applied Superconductivity* **26**, 1 (2016).
- [38] R. T. Kapur, P. Kehayias, S. K. Tolpygo, A. A. Libson, G. Haldeman, C. N. Muniz, A. Wynn, N. J. O’Connor, N. A. Parmar, R. Johnson, A. C. Maccabe, J. Cummings, J. L. Mallek, D. A. Braje, and J. M. Schloss, “Flux trapping characterization for superconducting electronics using a cryogenic widefield nv-diamond microscope,” (2025), [arXiv:2506.01906 \[cond-mat.supr-con\]](https://arxiv.org/abs/2506.01906).
- [39] K. Likharev, *Radiophysics and Quantum Electronics* **14**, 722 (1971).
- [40] C. Bean and J. Livingston, *Physical Review Letters* **12**, 14 (1964).
- [41] K. H. Kuit, J. R. Kirtley, W. van der Veur, C. G. Moleenaar, F. J. G. Roesthuis, A. G. P. Troeman, J. R. Clem, H. Hilgenkamp, H. Rogalla, and J. Flokstra, *Phys. Rev. B* **77**, 134504 (2008).
- [42] K. H. Kuit, J. R. Kirtley, J. R. Clem, H. Rogalla, and J. Flokstra, *IEEE Transactions on Applied Superconductivity* **19**, 3537 (2009).
- [43] G. Stan, S. B. Field, and J. M. Martinis, *Phys. Rev. Lett.* **92**, 097003 (2004).
- [44] G. Mkrtchyan and V. Shmidt, *Soviet Physics JETP* **34**, 195 (1972).
- [45] V. V. Schmidt and G. S. Mkrtchyan, *Soviet Physics Uspekhi* **17**, 170 (1974).
- [46] A. I. Buzdin, *Physical Review B* **47**, 11416 (1993).
- [47] A. Buzdin and D. Feinberg, *Physica C: Superconductivity* **235**, 2755 (1994).
- [48] H. Nordborg and V. Vinokur, *Physical Review B* **62**, 12408 (2000).

- [49] M. M. Doria and G. F. Zebende, *Physical Review B* **66**, 064519 (2002).
- [50] M. M. Doria, S. C. de Andrade, and E. Sardella, *Physica C: Superconductivity* **341**, 1199 (2000).
- [51] A. Bezryadin, Y. N. Ovchinnikov, and B. Pannetier, *Physical Review B* **53**, 8553 (1996).
- [52] V. Ginzburg and L. Landau, *Zh. Eksp. Teor. Fiz* **20**, 1064 (1950).
- [53] V. L. Ginzburg, in *Doklady Akademii Nauk*, Vol. 118 (Russian Academy of Sciences, 1958) pp. 464–467.
- [54] M. Tinkham, *Introduction to superconductivity* (Courier Corporation, 2004).
- [55] J. Bardeen, *Reviews of modern physics* **34**, 667 (1962).
- [56] E. H. Brandt, *Physical Review B—Condensed Matter and Materials Physics* **72**, 024529 (2005).
- [57] Y. Mawatari, *Physical Review B* **54**, 13215 (1996).
- [58] J. Pearl, *Applied Physics Letters* **5**, 65 (1964).
- [59] S. K. Tolpygo, V. Bolkhovsky, D. E. Oates, R. Rastogi, S. Zarr, A. L. Day, T. J. Weir, A. Wynn, and L. M. Johnson, *IEEE Transactions on Applied Superconductivity* **28**, 1 (2018).